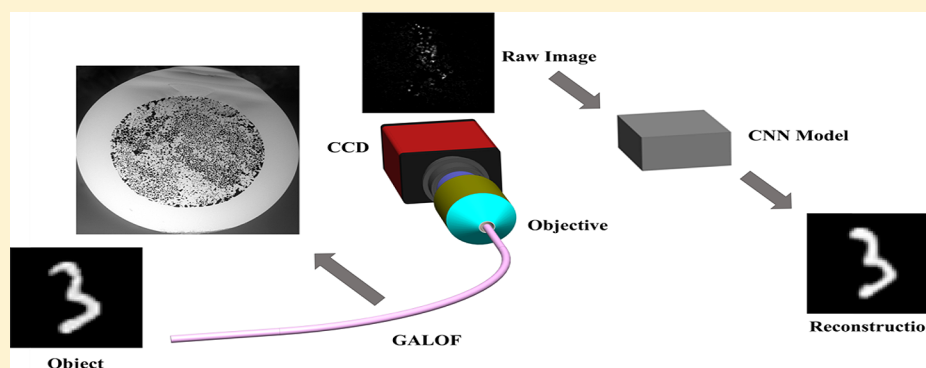# Deep Learning Imaging through Fully-Flexible Glass-Air Disordered Fiber

Jian Zhao,*[†] Yangyang Sun,[†] Zheyuan Zhu, Jose Enrique Antonio-Lopez, Rodrigo Amezcua Correa, Shuo Pang, and Axel Schülzgen

CREOL, The College of Optics and Photonics, University of Central Florida, Orlando, Florida 32816, United States

Ⓢ *Supporting Information*

ABSTRACT: We demonstrate a fully flexible, artifact-free, and lensless fiber-based imaging system. For the first time, this system combines image reconstruction by a trained deep neural network with low-loss image transmission through disordered glass-air Anderson localized optical fiber. We experimentally demonstrate transmission of intensity images through meter-long disordered fiber with and without fiber bending. The system provides the unique property that the training performed within a straight fiber setup can be utilized for high fidelity reconstruction of images that are transported through either straight or bent fiber making retraining for different bending situations unnecessary. In addition, high quality image transport and reconstruction is demonstrated for objects that are several millimeters away from the fiber input facet eliminating the need for additional optical elements at the distal end of the fiber. This novel imaging system shows great potential for practical applications in endoscopy including studies on freely behaving subjects.

KEYWORDS: *transverse Anderson localization, microstructured optical fiber, fiber imaging, lensless imaging, convolutional neural network*

Fiber optical endoscopes (FOEs) are very important and widely used tools in biomedical research, clinical diagnostics and surgical operations.[1,2] They enable imaging under conditions in which conventional microscopy cannot work well. For example, FOE-based optical imaging can be performed for cells reside within hollow tissue tracts or deep within organs in a minimally invasive way, while those locations are inaccessible for conventional microscopy.[2,3] Furthermore, FOEs can be implanted within freely behaving subjects, such as mice, for long-term imaging research.[4,5] This ability can benefit several areas, such as fundamental biological research and application research in developing in vivo methods for drug testing. Different types of fibers have been proposed for FOEs.[1] However, current solutions suffer from several limitations regarding system complexity and size, image quality and bending sensitivity. For example, single mode fibers can be used as the smallest imaging acquisition unit, but a mechanical scanning head or a spectral encoding device is often installed at the distal end of the fiber to deliver 2D imaging information, which makes the system bulky and

complex.[1,6,7] Alternatively, commercially available fiber bundles are able to transport 2D imaging information directly through FOEs. However, pixelation artifacts dictated by the individual cores fundamentally limit the transported image quality. In addition, any crosstalk between fiber cores in the bundle blurs the transmitted images[8] and the cost of materials and fabrication of fiber bundles is rather high.[9] Instead of utilizing thousands of fiber cores, the thousands of different spatial modes in multimode fiber (MMF) can also be used to transmit 2D imaging information. Current MMF based FOEs mainly rely on compensating randomized phases by wavefront shaping after calibrating the transmission matrix (TM) of the fiber.[5,10−14] This method suffers from several limitations. The most critical one is its intolerance to fiber movement. Any tiny movement or bending of the MMF will change the TM resulting in impaired imaging unless recalibration is performed, or very precise knowledge of the bending and its shape is

available.[14] TM recalibration requires open optical access to the distal end of the MMF and is fairly time-consuming.

Recent progress in light transmission through disordered optical fibers mediated by transverse Anderson localization opens a new avenue for improving the performance of FOEs.[15−22] The glass-air Anderson localized optical fiber (GALOF) was predicted to be an ideal candidate for imaging purposes.[17,18] The GALOF can support thousands of modes in its random structure, and unlike MMF, most of these modes show bending-independent single mode properties.[19] In fact, each mode embedded in the disordered optical fiber corresponds to a beam transmission channel formed by a multiple scattering process.[18,19] Due to its intriguing properties, the GALOF demonstrates several advantages over conventional fiber. First, bending-independent imaging can be performed without any extra lens or mechanical parts if the object is positioned adjacent to the input facet of the GALOF.[17,21,22] Second, GALOF can also directly transport high quality intensity images, and recent progress has confirmed that the image quality obtained after transport through meter-long GALOFs can be comparable to or better than that of images transmitted through some of the best commercial fiber bundles.[22] Moreover, meter-long imaging transmission distance can be achieved by GALOF due to its low attenuation below 1 dB per meter for visible wavelengths. Besides the superior imaging performance, required materials and fabrication processes of GALOFs promise potentially low cost.

The current GALOF-based FOEs still face a number of challenges to become preeminent FOEs that are fully flexible, artifact-free, and lensless. The structural parameters of current GALOFs determined by the applied fabrication process are still less than perfect, which limits the image quality. Moreover, to achieve a decent transferred image quality, the image plane needs to be located in the direct vicinity of the GALOF's input facet. Thanks to the recently burgeoning deep learning technology,[23] it is possible to address these challenges and create a fully flexible and lensless FOEs that delivers artifact-free, high quality images by combining GALOFs with deep learning algorithms. Deep learning is a recent rapidly growing research field that has already being applied to solve numerous imaging-related problems.[23−28] Contrary to conventional methods of solving the imaging optimization problem, the CNN can learn the forward operator and the regularizer implicitly through a training process without requiring prior knowledge of them. For example, to describe the image reconstruction process, we could assume that the object intensity image I_{obj}, and the fiber-transported raw intensity image I_{raw} are related by $I_{raw} = HI_{obj}$, where H denotes the forward operator connecting the input object image and the measured raw image. To reconstruct the object I_{rec}, one way is to solve an optimization problem of the form:

$$\tilde{I}_{rec} = \underset{I_{rec}}{\arg\min} \|HI_{rec} - I_{raw}\|^2 + \gamma\varphi(I_{rec}) \tag{1}$$

where φ is the regularizer encoding the prior knowledge of the object, and γ is the regularization parameter that adjusts the relative strength of the two terms in the optimization process.[29,30] The problem of this method is that it requires precise knowledge of H and proper selection of φ. For the transmission through our complex disordered imaging fiber, it is very difficult to develop an accurate physics model of this type, and the simulation process requires huge computational

power.[31] And deep learning demonstrates its superiority since it does not require prior knowledge and just needs the computational power of a PC for this work.

Here, we apply a particular type of deep neural network, called a convolutional neural network (CNN), to address the challenges facing GALOF-based FOEs. We demonstrate that an imaging system combining a CNN and a GALOF does not need any distal optics to transport 2D imaging information at various working distances. Therefore, the diameter of the FOEs could be reduced to the diameter of the fiber itself. Besides that, the imaging quality is improved by the CNN to the artifact-free level. Moreover, by combing the bending-independent properties of the GALOF with CNN based reconstruction, meter-long distance fully flexible imaging transportation is achieved.

The experimental setup is shown in Figure 1. The GALOF used here was fabricated at CREOL using fused-silica tubes
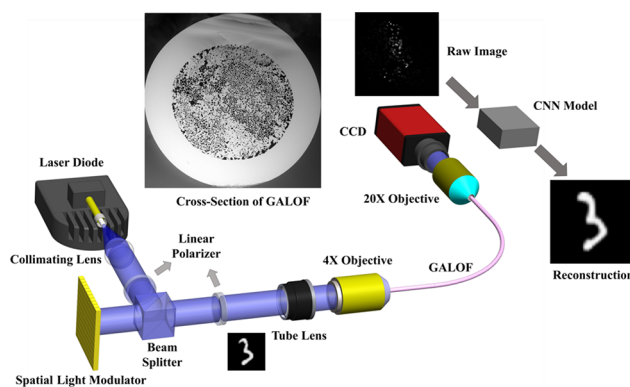

Figure 1. Schematic of the experimental setup.

and the stack-and-draw fabrication method.[22] The diameter of the random structure is about 278 μm, and the air-hole-filling fraction in the random structure is approximately 28.5%. The total length of the GALOF is 90 cm, and the spatial resolution provided by this sample is about 14 μm, see section 1 in Supporting Information. Using a shorter 4.5 cm long sample, the resolution can be improved to about 8 μm.

For our object generation we use 405 nm laser light that is delivered by a single mode fiber and collimated by a lens (50 mm focal length). A spatial light modulator (SLM) is located in between two linear polarizers to create an intensity object using its individual pixels. The light goes through the first polarizer oriented at 45° with respect to the extraordinary axis of the SLM. After reflection from SLM, the beam transmits through the second polarizer with the same polarization orientation as the first one. The SLM pixel size is 9.2 × 9.2 μm^2, and the number of pixels is 1920 × 1152. The SLM is modulated by 8-bit grayscale input images obtained from the Modified National Institute of Standards and Technology (MNIST) database of handwritten digits. The images created with the SLM were resized to a matrix of 56 × 56 pixels. Subsequently, the SLM images were demagnified by a factor of 4 and projected onto the GALOF input facet by the combination of a tube lens and a 4× objective. At the output end of the GALOF the fiber facet is projected onto a CCD camera (Manta G-145B) by a 20× objective. The CCD pixel size is 6.45 × 6.45 μm^2, and the number of pixels is 1388 × 1038. We crop the collected raw images to an 896 × 896 square for processing.

The CNN requires a training process to generate a computational architecture that accurately maps the images transported by the optical fiber to its original objects. Training of the CNN requires a large number of matched input (images of original objects) and output (the transported raw images) pairs to optimize the parameters of the neural network and build a suitable computational architecture. In addition, a separate set of image pairs serves as a test set to evaluate the performance of the trained CNN. When collecting data, we first send 4000 different images to the SLM and record the corresponding raw intensity images with the CCD camera. These 4000 image pairs, originally generated by the SLM and their corresponding CCD-recorded raw images, are used as the training set. Using the same setup, we collect another 500 pairs of different images that serve as our test set for the image reconstruction analysis.

The schematic of our CNN training and image reconstruction process is shown in Figure 2. Please see section 2 in
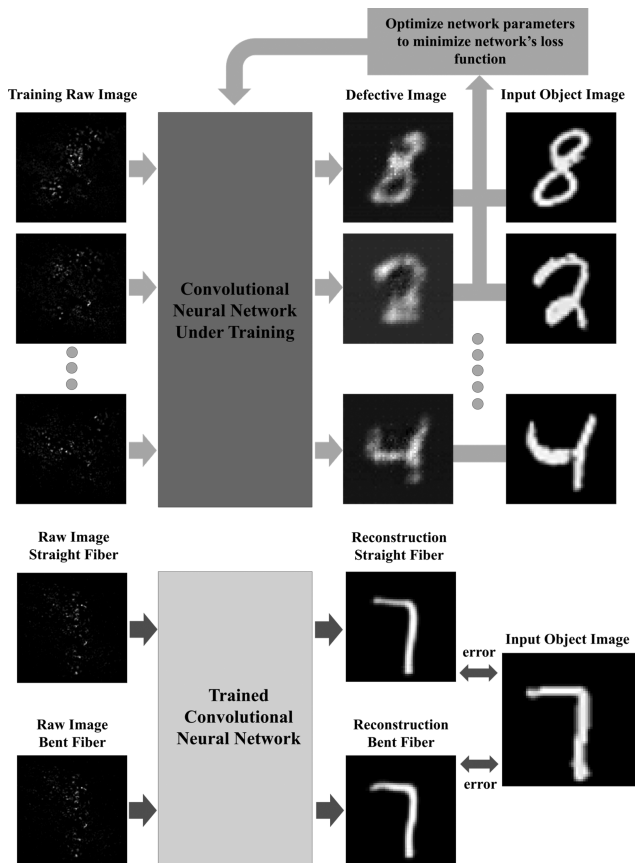
Figure 2. Schematic of the training and reconstruction process using a deep convolutional neural network.

Supporting Information for the detailed architecture of our CNN. In the training phase (with randomly initialized parameters), a set of raw images are sent into the CNN to obtain defective output images. The CNN is trained by optimizing its parameters through minimizing the loss function between these defective output images and their corresponding input images. This training procedure takes about 38 min using two GPUs (NVIDIA GeForce 1080Ti). After the training, the parameters of our CNN are fixed, and the CNN is applied to reconstruct new images from the raw images of our test set. The bottom part of Figure 2 demonstrates that the trained

CNN can be used to obtained high quality artifact-free reconstructed images from our test set raw images. The reconstruction time is only 4 ms for each test image. This shows the potential to perform in vivo video-rate real-time reconstruction of moving samples such as cells or neurons. To quantify the performance of the CNN, we compare the reconstructed images with the corresponding input images by the mean absolute error (MAE) method. The MAE is defined as $|\tilde{I}_{rec} - I_{obj}|/(wh)$, where w and h are the width and height of the image.

As a next step, we investigate how bending of the fiber influences our image reconstruction ability. As shown in the bottom part of Figure 2, and later in more detail in Figure 4, the same CNN, trained using straight GALOF, can be applied to reconstruct images transferred through both straight GALOF and GALOF with a 90° bend with high fidelity. This is in striking contrasts to image reconstruction using the TM method after transmission through MMF. As stated earlier, any slight movement or bending of the MMF requires recalibration of the TM. In addition, any recalibration requires access to the distal end of the fiber prohibiting monitoring of freely behaving subjects using the TM method and MMF for image transfer. In our approach, a trained CNN can be applied to reconstruct high quality images from raw images after transfer through bent GALOF in real time and without any retraining or any knowledge about the bending shape even for very large fiber bending angles.

Examples of reconstruction results from raw images measured after transport through straight GALOF are shown in Figure 3. The data shown in Figure 3a−c are collected at different imaging depths, that is, at different distances between the GALOF input facet and the imaging plane, ranging from 0 to 4 mm. The general CNN architecture used for reconstruction at the three different depths is the same. However, the CNNs are trained for each depth individually resulting in depth specific CNN parameters. Comparing input images and the corresponding reconstructed images, it is apparent that our trained CNNs are able to recover the true images remarkably well. Moreover, the imaging plane of our system is not limited to a specific depth. Without extra distal end optics, for objects located between 0 and 4 mm from the fiber facet, our system can perform high quality image transportation and reconstruction. We also demonstrate reconstruction results of ten different writing styles of the same number at three different depths, see section 4 in Supporting Information. Although the objects from the MNIST database used in Figure 3 and Figures S5−S7 are relatively simple, there should be no limitations on the complexity of the objects for the imaging system to perform well. Imaging of more complex objects, such as biological tissue, is part of ongoing research but is beyond the scope of this proof-of-concept work. An object distance of 4 mm represents an order of magnitude improvement compared to recently reported MMF-based imaging.[5] Being able to "see" objects at considerable distance from the fiber facet without any imaging elements will reduce the size of the imaging device to the diameter of the fiber itself. Therefore, endoscopes based on our system can be operated in a minimally invasive manner dramatically decreasing the risk of damage, for instance, to human organs. This is also important in in vivo studies of neural activity since there is a good chance to damage the neurons close to the fiber tip.
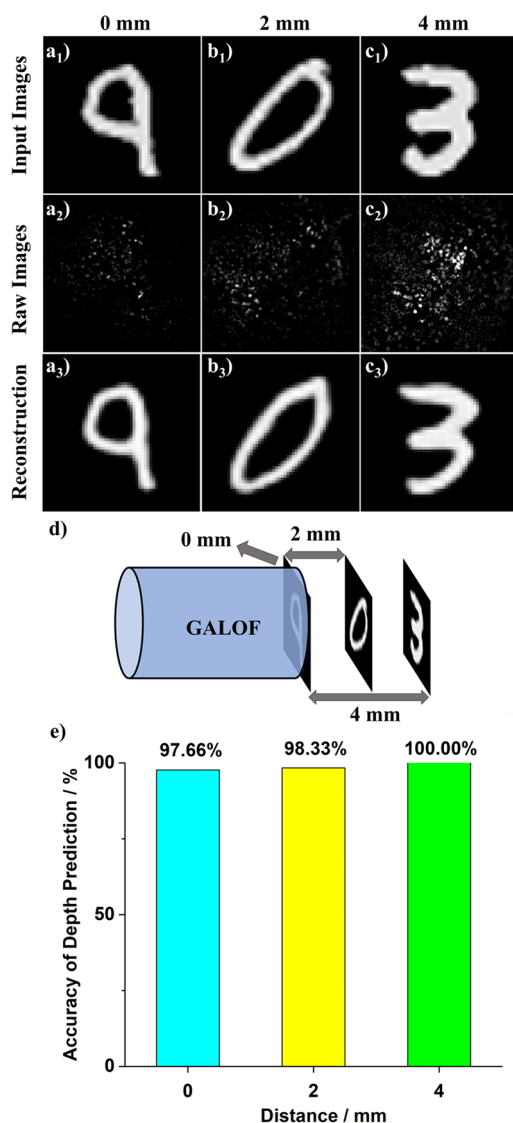
Figure 3. (a_1), (b_1), and (c_1) are input object images from the MNIST database; (a_2), (b_2), and (c_2) are the corresponding raw intensity images transmitted through a 90 cm long straight GALOF segment; (a_3), (b_3), and (c_3) are reconstructed images from the raw images. As illustrated in (d), (a_1)−(a_3) are obtained when the imaging depth (the distance between the image plane and the GALOF input facet) is 0 mm; (b_1)−(b_3) are obtained for 2 mm depth; (c_1)−(c_3) are obtained for 4 mm depth. (e) Probability that the deep neural network model can recognize correctly the imaging depth of the object from the measured raw image. These are statistical data obtained from the sets of 500 test samples used for the respective distances.

We also explore the possibility of predicting the depth of an object using the GALOF-transported raw images. For this purpose, we introduce a CNN classification model, see section 3 in Supporting Information for more technical details. After finishing the training process, this CNN is able to predict the image depth within a particular depth set, here 0, 2, or 4 mm. Although the input images corresponding to different depth are randomly mixed, the trained CNN is able to predict the depth of the images with remarkable accuracy, close to 100%, see Figure 3e. We study the depth prediction capability of our system in more detail using a separate 4.5 cm long GALOF sample, see section 3 in Supporting Information, where we
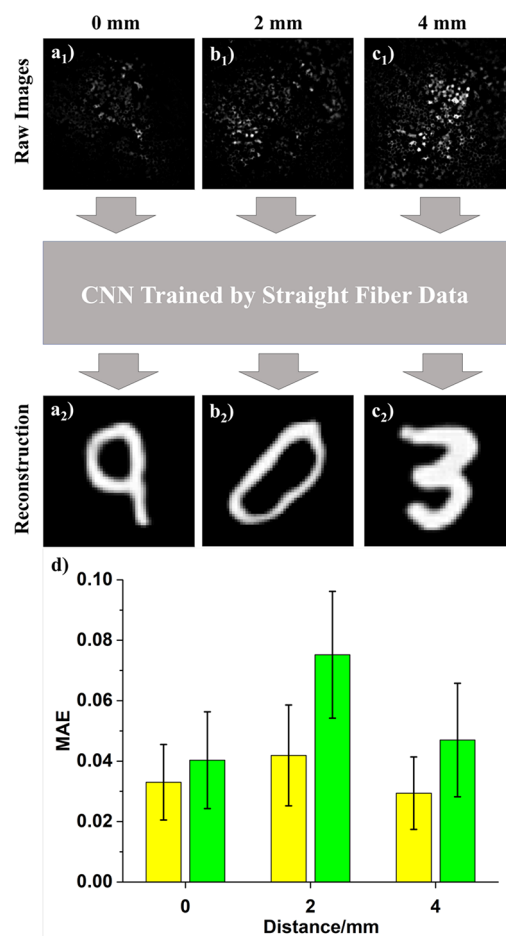

Figure 4. (a)−(c) Imaging reconstruction results for the same 90 cm GALOF segment bent by 90°. (a), (b), and (c) correspond to different image depths of 0, 2, and 4 mm, respectively. The input images are not shown here, but they are the same as those displayed inFigure 3. (a_1), (b_1), and (c_1) are three raw images collected after the GALOF. (a_2), (b_2), and (c_2) are the corresponding reconstructed images. (d) Error analysis for both straight GALOF and bent GALOF. Yellow and green bars correspond to the cases without and with bending, respectively.

report the sorting of images into six depth categories ranging from 0 to 10 mm. The averaged probability of accurately predicting the depth is 86.29% for this short GALOF sample. Beyond the demonstrated ability of obtaining good images of objects that are several millimeters away from the fiber facet, the depth prediction capability provides a first step toward the reconstruction of images with a remarkable depth resolution.

As indicated in Figure 2, the CNN trained to reconstruct images from straight fiber can be used directly to perform reconstruction for bent GALOF. As is demonstrated in Figure 4, this bending independence of the GALOF/CNN imaging system also applies to large imaging depths. Since the bending independence is mainly due to the single-mode properties of the transmission channels embedded in the GALOF, the transmission should stay the same for arbitrary bent states. Without losing of generality, we bend the GALOF by 90° and collect the test raw imaging data for object depths of 0, 2, and 4 mm, respectively. As illustrated in Figure 4a−c, high quality images can be recovered by feeding raw test images of low quality into the CNN model. Please note that these raw test images of different depth are obtained after transport through

bent GALOF, while the CNN training was performed using straight GALOF. For a quantitative analysis, bar graphs are plotted in Figure 4d that show the MAE and its statistics for test data sets of different depths transferred through straight (yellow bars) and bent GALOF (green bars). The low test errors for all cases suggest that our CNN has learned a model of underlying physics of the imaging system and can generate highly accurate results. The slightly higher test error for bending fiber might be attributed to the experimental process that requires movement and readjustment of the imaging setup located at the output side of the GALOF. For MMF-based fiber imaging, a few hundred micrometers perturbations are already strong enough to impair the image quality. Compared to that extreme bending-sensitivity of MMF, our system is totally free from the impact of strong bending. This ability would make our system an ideal candidate for a fully flexible medical endoscope used in clinical diagnostics.

To demonstrate a broader imaging capability even for objects belonging to different classes, we reconstruct English letters using the same CNN model trained by a straight GALOF and the MNIST database of handwritten digits, see Figure 5. English letters are a member of a totally different
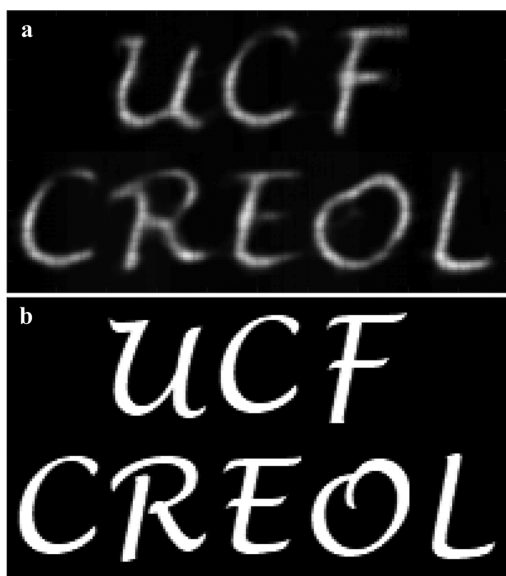
Figure 5. Reconstruction result of English letters: (a) is the reconstruction image; (b) is the object image. The object image is projected into the straight GALOF facet with 0 mm depth.

domain compared to the numbers in the MNIST data set. We pick the letters UCF (short for "University of Central Florida") and CREOL (short for "College of Optics and Photonics") as the object. The image size of the object is 112×200 pixels. Limited by the size of the GALOF diameter, we have to scan the object and stitch the subsets together to obtain the complete images shown in Figure 5a. The comparison between the reference and the recovered image demonstrates that our system is able to accurately reconstruct images belonging to a very different class. This is further strong evidence that our CNN is an accurate estimate of the physics model. Therefore, the imaging capability of our system generalizes well through objects of different classes.

In conclusion, we demonstrate a fully flexible and artifact-free fiber-based imaging system with a meter-long GALOF at multiple working distances up to several millimeters. There are

several fundamental aspects that set our system apart from other approaches, most notably the bending independence of the network training process and the large object depth that have been achieved without the need for distal optical elements. Our system's tolerance to flexible bending and long working distances will be of enormous benefit for both basic research on biological and disease processes and practical application in clinical diagnostics and surgical operations. As the next step of demonstrating the potential of our imaging system, we will replace SLM generated images with real biological samples. Besides that, we believe that we can further improve our deep neural network model. One future goal is to develop an integrated model to perform depth prediction and image reconstruction with a one-time trained network, which would open the door for real-time image transmission and reconstruction with depth resolution using GALOF/CNN based imaging systems.

◼ METHODS

GALOF Fabrication. The GALOF is fabricated by the well-known stack and draw method.[22] Thousands of silica capillary tubes are fabricated with different outer diameter as well as different ratio of inner diameter (ID) to outer diameter (OD). The OD of the silica capillaries ranges from ∼100 to ∼180 μm and the ID/OD ranges from 0.5 to 0.8. The capillaries are mixed randomly and fed into a jacket to make the perform. Once the preform is completed, it is drawn to canes with around 3 mm outer diameter. Subsequently, the cane is drawn to the desired fiber size. The air-hole areas in the GALOF range from 0.64 μm^2 to over 100 μm^2. Statistically, areas of approximately 2.5 μm^2 cover the largest area of the randomly disordered region of GALOF.[22] The measured attenuation at visible wavelengths is below 1 dB per meter.

◼ ASSOCIATED CONTENT

ⓢ Supporting Information

The Supporting Information is available free of charge on the ACS Publications website at DOI: 10.1021/acsphotonics.8b00832.

Section 1: Resolution measurement. Section 2: CNN architecture for reconstruction. Section 3: CNN Architecture for depth prediction. Section 4: Reconstruction results at different imaging depths (PDF).

◼ AUTHOR INFORMATION

Corresponding Author
*E-mail: jianzhao@knights.ucf.edu.

ORCID ⓞ
Jian Zhao: 0000-0002-3947-4049

Author Contributions
[†]These authors contributed equally.

Notes
The authors declare no competing financial interest.

◼ REFERENCES

(1) Flusberg, B. A.; Cocker, E. D.; Piyawattanametha, W.; Jung, J. C.; Cheung, E. L.; Schnitzer, M. J. Fiber-optic fluorescence imaging. *Nat. Methods* **2005**, *2* (12), 941−50.

(2) Koenig, F.; Knittel, J.; Stepp, H. Diagnosing Cancer in Vivo. *Science* **2001**, *292* (5520), 1401.

(3) Yelin, D.; Rizvi, I.; White, W. M.; Motz, J. T.; Hasan, T.; Bouma, B. E.; Tearney, G. J. Three-dimensional miniature endoscopy. *Nature* **2006**, *443*, 765.

(4) Szabo, V.; Ventalon, C.; De Sars, V.; Bradley, J.; Emiliani, V. Spatially Selective Holographic Photoactivation and Functional Fluorescence Imaging in Freely Behaving Mice with a Fiberscope. *Neuron* **2014**, *84* (6), 1157−1169.

(5) Ohayon, S.; Caravaca-Aguirre, A.; Piestun, R.; DiCarlo, J. J. Minimally invasive multimode optical fiber microendoscope for deep brain fluorescence imaging. *Biomed. Opt. Express* **2018**, *9* (4), 1492−1509.

(6) Ducourthial, G.; Leclerc, P.; Mansuryan, T.; Fabert, M.; Brevier, J.; Habert, R.; Braud, F.; Batrin, R.; Vever-Bizet, C.; Bourg-Heckly, G.; Thiberville, L.; Druilhe, A.; Kudlinski, A.; Louradour, F. Development of a real-time flexible multiphoton microendoscope for label-free imaging in a live animal. *Sci. Rep.* **2016**, *5*, 18303.

(7) Barankov, R.; Mertz, J. High-throughput imaging of self-luminous objects through a single optical fibre. *Nat. Commun.* **2014**, *5*, 5581.

(8) Reichenbach, K. L.; Xu, C. Numerical analysis of light propagation in image fibers or coherent fiber bundles. *Opt. Express* **2007**, *15* (5), 2151−2165.

(9) Stone, J. M.; Wood, H. A. C.; Harrington, K.; Birks, T. A. Low index contrast imaging fibers. *Opt. Lett.* **2017**, *42* (8), 1484−1487.

(10) Čižmár, T.; Dholakia, K. Shaping the light transmission through a multimode optical fibre: complex transformation analysis and applications in biophotonics. *Opt. Express* **2011**, *19* (20), 18871−18884.

(11) Caravaca-Aguirre, A. M.; Niv, E.; Conkey, D. B.; Piestun, R. Real-time resilient focusing through a bending multimode fiber. *Opt. Express* **2013**, *21* (10), 12881−12887.

(12) Cizmar, T.; Dholakia, K. Exploiting multimode waveguides for pure fibre-based imaging. *Nat. Commun.* **2012**, *3*, 1027.

(13) Choi, Y.; Yoon, C.; Kim, M.; Yang, T. D.; Fang-Yen, C.; Dasari, R. R.; Lee, K. J.; Choi, W. Scanner-Free and Wide-Field Endoscopic Imaging by Using a Single Multimode Optical Fiber. *Phys. Rev. Lett.* **2012**, *109* (20), 203901.

(14) Plöschner, M.; Tyc, T.; Čižmár, T. Seeing through chaos in multimode fibres. *Nat. Photonics* **2015**, *9* (8), 529−535.

(15) Schwartz, T.; Bartal, G.; Fishman, S.; Segev, M. Transport and Anderson localization in disordered two-dimensional photonic lattices. *Nature* **2007**, *446* (7131), 52−55.

(16) Karbasi, S.; Mirr, C. R.; Yarandi, P. G.; Frazier, R. J.; Koch, K. W.; Mafi, A. Observation of transverse Anderson localization in an optical fiber. *Opt. Lett.* **2012**, *37* (12), 2304−2306.

(17) Karbasi, S.; Frazier, R. J.; Koch, K. W.; Hawkins, T.; Ballato, J.; Mafi, A. Image transport through a disordered optical fibre mediated by transverse Anderson localization. *Nat. Commun.* **2014**, *5*, na.

(18) Mafi, A. Transverse Anderson localization of light: a tutorial. *Adv. Opt. Photonics* **2015**, *7* (3), 459−515.

(19) Ruocco, G.; Abaie, B.; Schirmacher, W.; Mafi, A.; Leonetti, M. Disorder-induced single-mode transmission. *Nat. Commun.* **2017**, *8*, 14571.

(20) Abaie, B.; Mobini, E.; Karbasi, S.; Hawkins, T.; Ballato, J.; Mafi, A. Random lasing in an Anderson localizing optical fiber. *Light: Sci. Appl.* **2017**, *6*, e17041.

(21) Zhao, J.; Antonio-Lopez, J. E.; Correa, R. A.; Mafi, A.; Windeck, M.; Schülzgen, A. *Image Transport Through Silica-Air Random Core Optical Fiber, Conference on Lasers and Electro-Optics*, San Jose, California, 2017/05/14; Optical Society of America: San Jose, CA, 2017; p JTu5A.91.

(22) Zhao, J.; Lopez, J. E. A.; Zhu, Z.; Zheng, D.; Pang, S.; Correa, R. A.; Schülzgen, A. Image Transport Through Meter-Long Randomly Disordered Silica-Air Optical Fiber. *Sci. Rep.* **2018**, *8* (1), 3065.

(23) LeCun, Y.; Bengio, Y.; Hinton, G. Deep learning. *Nature* **2015**, *521* (7553), 436−44.

(24) Dong, C.; Loy, C. C.; He, K.; Tang, X. Image Super-Resolution Using Deep Convolutional Networks. *IEEE Trans Pattern Anal Mach Intell* **2016**, *38* (2), 295−307.

(25) Sinha, A.; Lee, J.; Li, S.; Barbastathis, G. Lensless computational imaging through deep learning. *Optica* **2017**, *4* (9), 1117−1125.

(26) Rivenson, Y.; Göröcs, Z.; Günaydin, H.; Zhang, Y.; Wang, H.; Ozcan, A. Deep learning microscopy. *Optica* **2017**, *4* (11), 1437−1443.

(27) Schlemper, J.; Caballero, J.; Hajnal, J. V.; Price, A. N.; Rueckert, D. A Deep Cascade of Convolutional Neural Networks for Dynamic MR Image Reconstruction. *IEEE Trans Med. Imaging* **2018**, *37* (2), 491−503.

(28) Rivenson, Y.; Ceylan Koydemir, H.; Wang, H.; Wei, Z.; Ren, Z.; Günaydin, H.; Zhang, Y.; Göröcs, Z.; Liang, K.; Tseng, D.; Ozcan, A. Deep Learning Enhanced Mobile-Phone Microscopy. *ACS Photonics* **2018**, *5*, 2354.

(29) Sun, Y.; Yuan, X.; Pang, S. High-speed compressive range imaging based on active illumination. *Opt. Express* **2016**, *24* (20), 22836−22846.

(30) Sun, Y.; Yuan, X.; Pang, S. Compressive high-speed stereo imaging. *Opt. Express* **2017**, *25* (15), 18182−18190.

(31) Karbasi, S.; Mirr, C. R.; Frazier, R. J.; Yarandi, P. G.; Koch, K. W.; Mafi, A. Detailed investigation of the impact of the fiber design parameters on the transverse Anderson localization of light in disordered optical fibers. *Opt. Express* **2012**, *20* (17), 18692−18706.